INTERNATIONAL JOURNAL OF
NUMERICAL ANALYSIS AND MODELING
Volume 18, Number 2, Pages 165–189

ENERGY AND ENSTROPHY STUDY OF THE TIME RELAXATION MODEL

TAHJ HILL, MONIKA NEDA, ERIC OLSON, AND FARANAK PAHLEVANI

Abstract. This paper presents an investigation of the convergence of an Oseen type of problem for a fluid model known as Time Relaxation Model, TRM. Furthermore conservation of energy and enstrophy of TRM are presented along with a dimensional analysis study of these properties. The paper contains two types of numerical experiments, one of which is based on finite element discretization that employs the Oseen type of problem for dealing with the nonlinearity of the TRM. The second type is the spectral related tests for the study of TRM dimensional analysis. Our numerical experiments confirm the theoretical findings.

Key words. Time relaxation, finite element, spectral method, energy, enstrophy.

1. Introduction

All the turbulent fluid models aim to create a balance between an accurate description of the fluid flow and the model resolution so that the simulation can be performed within a realistic time limits while the capacity set by today's high performing computers is also taken into consideration, [13, 16, 27]. This is due to the fact that at high Reynolds numbers the fluid's velocity $\mathbf{u}$ has many small spatial scales, which becomes computationally less feasible by standard NSE. Ultimately a very fine mesh is needed to capture all the small scales [1, 12, 11]. In this context, high order fluid models are of interest, since they deliver a more accurate simulation at low model resolution. However, generally speaking, all such models run the risk of altering the largest structures of the flow that contain most of the flow's energy and are responsible for most of the mixing and flow's momentum transport [21].

In the present paper the numerical properties of TRM are investigated including the conservative and spectral behavior in three-dimensional incompressible flows. This fluid model was first introduced by Stolz, Adams and Kleiser [28, 29]. The truncation scale analysis of TRM is shown in [21]. Further numerical studies and computational accuracy of this model can be found in [9, 11, 21, 24]. Parameter sensitivity analysis of TRM was performed in [25, 8].

The governing equations for TRM are formulated as

$$\begin{aligned} \mathbf{u}_t + \mathbf{u}\cdot\nabla\mathbf{u} - \nu\Delta\mathbf{u} + \nabla p + \chi(\mathbf{u}-\bar{\mathbf{u}}) &= \mathbf{f}, \\ \nabla\cdot\mathbf{u} &= 0, \end{aligned} \tag{1}$$

in the physical domain Ω, with either no-slip Dirichlet boundary conditions or periodic boundary conditions with zero spatial averages. Here $\mathbf{u}$, p, $\mathbf{f}$, denote velocity, pressure and body force, respectively, ν is the kinematic viscosity, χ is a scalar constant known as the relaxation parameter, and $\bar{\mathbf{u}}$ is the solution of the partial differential equation

$$-\delta^2\Delta\bar{\mathbf{u}} + \bar{\mathbf{u}} = \mathbf{u}, \tag{2}$$

where $\bar{\mathbf{u}}$ is subject to the same boundary conditions, either Dirichlet or periodic, as were applied to $\mathbf{u}$. In the above filtering equation, δ is a length scale corresponding

Received by the editors July 9, 2018 and, in revised form, September 23, 2020.
2000 *Mathematics Subject Classification.* 65M60, 65M70, 76F65.

to the filter width. Thus, for large δ values, $\bar{\mathbf{u}}$ is smooth and for small δ values, $\bar{\mathbf{u}}$ is close to $\mathbf{u}$. Continuous differential filters were introduced into fluid flow modeling by Germano [14] and used for various fluid flow regularizations, see, for example, [1, 4, 5, 15, 23].

The time relaxation parameter is considered to be a positive quantity, *i.e.*, $\chi > 0$, and has units of inverse time. The term $\chi(\mathbf{u}-\bar{\mathbf{u}})$ aims to drive the unresolved scales to zero exponentially [12]. In working with the TRM, the parameter χ must be specified and scaled appropriately in relation to other parameters in the problem [21].

This paper is organized as follows. In Section 2 we introduce notation and recall some standard results that will be used throughout. Section 3 examines the energy and enstrophy balance of the TRM. Note the energy analysis applies to dimensions $d = 2$ and 3 while enstrophy is considered only for $d = 2$. We show, see equations (11) and (16), that the average rate of dissipation of energy and enstrophy are both increased by a single term proportional to $\chi\delta^2$ compared to the NSE. After characterizing the energy spectrum based on a dimensional analysis of the corresponding inertial ranges for the energy and enstrophy cascades, the results of a fully-resolved spectral-Galerkin simulation are presented to check the dissipation and energy spectrum of the TRM. Note that details of the forcing used in this simulation are given in Appendix A.

Section 4 includes our main results on the practical use of the TRM in finite-element computations. Upon stating the weak formulation, we show that the resulting Oseen problem for the TRM can be approximated numerically using a globally convergent fixed-point iteration. We then compute the Taylor–Green vortex as a benchmark to compare the behavior of the TRM to known NSE dynamics. In particular, the approximate solution obtained by the TRM exhibited the enstrophy increase as desired as well as a near-constant normalized kinetic energy.

The same computational setup, but at a reduced Reynolds number, is then used to numerically solve the sensitivity equations for the TRM using different values of δ and χ. The numerics are found to be consistent with prior sensitivity analysis and illustrate some tradeoffs when tuning these parameters. The paper ends with our conclusions in Section 5 where we provide some additional remarks and also reflect on directions for future study.

2. Preliminaries and Notations

This section presents our functional spaces, preliminary results and notations used in our analysis. While both Dirichlet and periodic boundary conditions will be considered in this paper, we give details here only for the Dirichlet case and note, after accounting for the necessary modifications, that the periodic case is similar. The $L^2(\Omega)$ norm and inner product will be denoted by $\|\cdot\|$ and $(\cdot,\cdot)$. Likewise, the $L^p(\Omega)$ norms and the Sobolev $W_p^k(\Omega)$ norms are denoted by $\|\cdot\|_{L^p}$ and $\|\cdot\|_{W_p^k}$, respectively. H^k is used to represent the Sobolev space W_2^k, and $\|\cdot\|_k$ denotes the norm in H^k.

For functions $\mathbf{v}(\mathbf{x},t)$ defined on the entire time interval $(0,T)$, we define

$$\|\mathbf{v}\|_{\infty,k} := \sup_{0<t<T} \|\mathbf{v}(t,\cdot)\|_k \qquad \text{and} \qquad \|\mathbf{v}\|_{m,k} := \left(\int_0^T \|\mathbf{v}(t,\cdot)\|_k^m \, dt\right)^{1/m}.$$

Define

$$\mathbf{X} = H_0^1(\Omega) := \{\, \mathbf{v} \in H^1(\Omega) : \mathbf{v}|_{\partial\Omega} = 0 \,\},$$
$$Q = L_0^2(\Omega) := \{\, q \in L^2(\Omega) : \textstyle\int_\Omega q = 0 \,\},$$

We denote the dual space of $\mathbf{X}$ as $\mathbf{X}^*$, with norm $\|\cdot\|_*$. Given a function $\mathbf{f} \in L^2(\Omega)^d$, the $\mathbf{X}^*$ norm of $\mathbf{f}$ is defined as

$$\|\mathbf{f}\|_* := \sup_{\mathbf{v}\in\mathbf{X}} \frac{(\mathbf{f},\mathbf{v})}{\|\nabla\mathbf{v}\|}.$$

For any $0 < \epsilon < \infty$, and $\frac{1}{p} + \frac{1}{q} = 1$ with $1 \le p, q \le \infty$, the $L^p(\Omega)$ inner product satisfies Hölder's and Young's inequalities given below, respectively, as

$$(\mathbf{u},\mathbf{v}) \le \|\mathbf{u}\|_{L^p}\|\mathbf{v}\|_{L^q}, \tag{3}$$

$$(\mathbf{u},\mathbf{v}) \le \frac{\epsilon}{p}\|\mathbf{u}\|_{L^p}^p + \frac{\epsilon^{-(q/p)}}{q}\|\mathbf{v}\|_{L^q}^q. \tag{4}$$

Inequality (4) in case $p = 2$ is known as the Cauchy–Schwarz inequality. The Poincaré–Friedrichs inequality is used frequently through this paper and its proof can be found in [20].

Theorem 2.1. The Poincaré–Friedrichs Inequality. *There is a positive constant C_{PF} depending only on the domain Ω such that*

$$\|\mathbf{u}\| \le C_{PF}\|\nabla\mathbf{u}\| \qquad \textit{for every} \qquad \mathbf{u} \in \mathbf{X}.$$

Also, bilinear $a(\cdot,\cdot)\colon \mathbf{X}\times\mathbf{X} \to \mathbb{R}$ and trilinear $b^*(\cdot,\cdot,\cdot)\colon \mathbf{X}\times\mathbf{X}\times\mathbf{X} \to \mathbb{R}$ forms are defined as,

$$a(\mathbf{u},\mathbf{v}) := (\nabla\mathbf{u},\nabla\mathbf{v}),$$
$$b^*(\mathbf{u},\mathbf{v},\mathbf{w}) := \frac{1}{2}(\mathbf{u}\cdot\nabla\mathbf{v},\mathbf{w}) - \frac{1}{2}(\mathbf{u}\cdot\nabla\mathbf{w},\mathbf{v}).$$

Lemma 2.1. [19, 20] *For $\mathbf{u},\mathbf{v},\mathbf{w} \in \mathbf{X}$, the trilinear term $(\mathbf{u}\cdot\nabla\mathbf{v},\mathbf{w})$ can be bounded by*

$$(\mathbf{u}\cdot\nabla\mathbf{v},\mathbf{w}) \le C(\Omega)\,\|\mathbf{u}\|^{\frac{1}{2}}\,\|\nabla\mathbf{u}\|^{\frac{1}{2}}\,\|\nabla\mathbf{v}\|\,\|\nabla\mathbf{w}\|,$$
$$(\mathbf{u}\cdot\nabla\mathbf{v},\mathbf{w}) \le C(\Omega)\,\|\nabla\mathbf{u}\|\,\|\nabla\mathbf{v}\|\,\|\nabla\mathbf{w}\|.$$

The above bounds hold for $b^*(\cdot,\cdot,\cdot)$ as well.

We remark that the second inequality in Lemma 2.1 follows from the first by a simple application of Theorem 2.1. In particular, the constant $C(\Omega)$ which appears in the first is non-dimensional and depends only on the domain Ω, while for notational convenience, the constant $C(\Omega)$ appearing in the second also includes the dimensional factor $C_{PF}^{1/2}$.

Theorem 2.2. The Lax–Milgram Theorem. *Let $a(\cdot,\cdot)\colon \mathbf{X}\times\mathbf{X} \to \mathbb{R}$ be a continuous and coercive bilinear form, i.e.,*

$$a(\mathbf{u},\mathbf{v}) \le C_1\|\mathbf{u}\|_{\mathbf{X}}\|\mathbf{v}\|_{\mathbf{X}} \qquad \textit{for all} \qquad \mathbf{u},\mathbf{v} \in \mathbf{X},$$
$$a(\mathbf{u},\mathbf{u}) \ge C_2\|\mathbf{u}\|_{\mathbf{X}}^2 \qquad \textit{for all} \qquad \mathbf{u} \in \mathbf{X},$$

for positive constants C_1 and C_2, based on the respective definitions. Let $F\colon \mathbf{X} \to \mathbb{R}$ be a linear functional such that

$$F(\mathbf{v}) \le C\|\mathbf{v}\|_{\mathbf{X}} \qquad \textit{for all} \qquad \mathbf{v} \in \mathbf{X}.$$

Then, there is a unique solution $\mathbf{u} \in \mathbf{X}$ *satisfying*

$$a(\mathbf{u}, \mathbf{v}) = F(\mathbf{v}) \qquad \textit{for all} \qquad \mathbf{v} \in \mathbf{X}.$$

The following theorem is about bounds for the filtered quantities that are applied in the finite element analysis.

Lemma 2.2. *For* $\mathbf{v} \in \mathbf{X}$ *and* $\bar{\mathbf{v}}$ *the corresponding solution to* (2)*, we have the bounds*

$$\|\bar{\mathbf{v}}\| \leq \|\mathbf{v}\| \qquad \textit{and} \qquad \|\nabla\bar{\mathbf{v}}\| \leq \|\nabla\mathbf{v}\|.$$

Proof. It can be found in [9, 22]. □

3. Energy and Enstrophy in the Time Relaxation Model

In this section we assume periodic boundary conditions and present the energy and enstrophy balance of the TRM in Sections 3.2 and 3.3, respectively, following the derivation and work in [26]. As a result, one can observe as the model parameters χ and δ approach to zero that the average rate dissipation of both energy and enstrophy approach to that of the NSE. Section 3.4 recalls the method of dimensional analysis subsequently used to derive scaling properties of the energy spectrum in Section 3.5 resulting from the energy cascade and in Section 3.6 from the enstrophy cascade. These theoretical results on the dissipation and energy spectrum of the TRM and then compared to a highly-resolved spectral-Galerkin simulation in Section 3.7 after which we proceed to Section 4 on the practical use of the TRM in finite-element computations.

3.1. Fourier Analysis. Recall that the TRM is obtained by the addition of the relaxation term $\chi(\mathbf{u} - \bar{\mathbf{u}})$ to the incompressible Navier–Stokes equations. Before beginning our discussion of the energy balance, it is instructive to consider the Fourier analysis obtained by projecting the TRM onto the Fourier modes of a 2π-periodic domain as

$$\frac{d\mathbf{u}_k(t)}{dt} + B(\mathbf{u})_k + L_k\mathbf{u}_k = \mathbf{f}_k \qquad \text{with} \qquad \mathbf{u}(x,t) = \sum_{k\in\mathbf{Z}^3\setminus\{0\}} \mathbf{u}_k(t)e^{ik\cdot x} \tag{5}$$

where

$$B(\mathbf{u}) = P_\sigma(\mathbf{u}\cdot\nabla)\mathbf{u}, \qquad (P_\sigma\mathbf{u})_k = \mathbf{u}_k - k\frac{k\cdot\mathbf{u}_k}{|k|^2} \quad \text{and} \quad L_k = \nu|k|^2 + \chi\frac{\delta^2|k|^2}{1+\delta^2|k|^2}.$$

Note that we have assumed $\nabla\cdot\mathbf{f} = 0$ or equivalently $k\cdot\mathbf{f}_k = 0$ for simplicity.

In the Fourier representation (5) above, the relaxation term appears in the definition of L_k and has the effect of modifying the viscous dissipation at each wave number $|k|$. Figure 1 graphs the ratio $L_k/(\nu|k|^2)$ to illustrate how much greater the dissipation in the TRM is compared to the original Navier–Stokes equations. Intuitively, the relaxation term has the effect of increasing the apparent viscosity for wave numbers up to about $|k| \approx 1/\delta$ after which the relative amount of additional dissipation decreases and functions only as a damping term when $|k| \gg 1/\delta$.

Thus, the term $\chi(u - \bar{u})$ in the time relaxation model serves to increase the effective viscosity at the large scales while functioning as a damping term at the small scales. In particular, the TRM does not involve higher-order differential operators such as hyperviscosity and provides no additional regularization properties compared to the NSE that can be used, for example, to show the model is well posed for three-dimensional flows. While this is the opposite of what might seem analytically convenient, from a turbulence modeling point of view, since dissipating

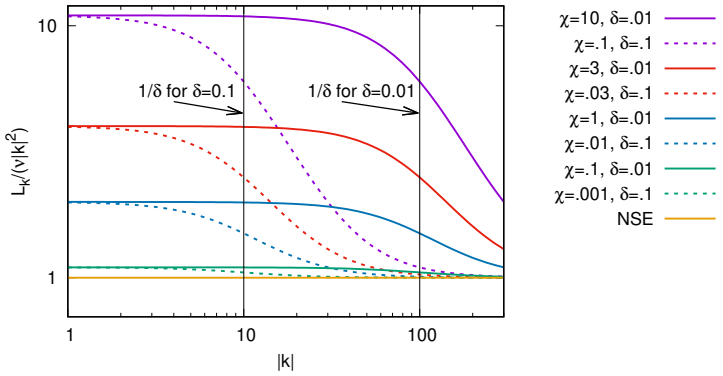

FIGURE 1. Fourier-space visualization of the filter $\chi(\mathbf{u}-\bar{\mathbf{u}})$ as the ratio of the dissipation L_k at wave number $|k|$ in the TRM over the corresponding viscous dissipation in the NSE. The solid and dotted lines of the same color represent parameter choices for which $\chi\delta^2$ are equal.

the small scales is the major role of viscosity, then it is arguably important for a turbulence model to have the correct physical viscosity at those scales. This suggests setting δ in the TRM to be on the order of the Kolmogorov length scale—the scale below which viscosity dominates and further connects δ to the size of the finite elements used in the practical fluid calculations of Section 4.

3.2. The Energy Balance. In these estimates it is assumed that the external force is zero, *i.e.*, $\mathbf{f} = 0$. To obtain the energy, first equation (1) is formally multiplied by the fluid velocity $\mathbf{u}$, then is integrated over the space Ω and time interval $[0, T]$ respectively. The first two steps yield the following equation:

$$\int_\Omega \mathbf{u}_t\cdot\mathbf{u}\,dx+\int_\Omega \mathbf{u}\nabla\mathbf{u}\cdot\mathbf{u}\,dx-\nu\int_\Omega \Delta\mathbf{u}\cdot\mathbf{u}\,dx+\int_\Omega \nabla p\cdot\mathbf{u}\,dx+\int_\Omega \chi(\mathbf{u}-\bar{\mathbf{u}})\cdot\mathbf{u}\,dx=0. \tag{6}$$

Using integration by parts, that $\nabla\cdot\mathbf{u}=0$ and the space periodicity of $\mathbf{u}$, one obtains

$$\int_\Omega \mathbf{u}\nabla\mathbf{u}\cdot\mathbf{u}\,dx=0, \qquad \int_\Omega \Delta\mathbf{u}\cdot\mathbf{u}\,dx=\|\nabla\mathbf{u}\|^2 \qquad \text{and} \qquad \int_\Omega \nabla p\cdot\mathbf{u}\,dx=0.$$

Therefore, equation (6) is reduced to

$$\frac{1}{2}\frac{d}{dt}\|\mathbf{u}\|^2+\nu\|\nabla\mathbf{u}\|^2+\chi\int_\Omega(\mathbf{u}-\bar{\mathbf{u}})\cdot\mathbf{u}\,dx=0. \tag{7}$$

At last, integration over the time interval $[0, T]$ brings us to the following equation:

$$\frac{1}{2}\|\mathbf{u}(T)\|^2+\int_0^T \nu\|\nabla\mathbf{u}\|^2dt+\int_0^T \chi\int_\Omega(\mathbf{u}-\bar{\mathbf{u}})\cdot\mathbf{u}\,dx\,dt=\frac{1}{2}\|\mathbf{u}(0)\|^2. \tag{8}$$

Note that equation (8) has the extra term $\int_0^T \chi\int_\Omega(\mathbf{u}-\bar{\mathbf{u}})\cdot\mathbf{u}\,dx\,dt$ compared to the NSE energy equation. In the following lemma we show that this term is a non-negative quantity; therefore it adds to the energy dissipation.

Lemma 3.1. *Suppose* $\mathbf{u}$ *and* $\bar{\mathbf{u}}$ *are solutions to the TRM with the corresponding model parameters* δ *and* χ*, then* $\int_\Omega(\mathbf{u}-\bar{\mathbf{u}})\cdot\mathbf{u}\,dx\geq 0$.

Proof. Based on the filtering equation (2),

$$\int_\Omega (\mathbf{u}-\bar{\mathbf{u}})\cdot\mathbf{u}\,dx = \int_\Omega -\delta^2\Delta\bar{\mathbf{u}}\cdot\mathbf{u}\,dx = \int_\Omega -\delta^2\Delta\bar{\mathbf{u}}\cdot(-\delta^2\Delta\bar{\mathbf{u}}+\bar{\mathbf{u}})\,dx. \tag{9}$$

Rewriting and applying the integration by parts yields

$$\int_\Omega (\mathbf{u}-\bar{\mathbf{u}})\cdot\mathbf{u}\,dx = \delta^4\int_\Omega \|\Delta\bar{\mathbf{u}}\|^2 dx + \delta^2\int_\Omega \|\nabla\bar{\mathbf{u}}\|^2\,dx. \tag{10}$$

The proof is complete by noting that the right-hand side quantities are nonnegative. □

In this paper, we denote the average TRM-enhanced rate of energy dissipation by ϵ defined as

$$\epsilon = \frac{1}{T|\Omega|}\Big\{\int_0^T \nu\|\nabla\mathbf{u}\|^2 dt + \int_0^T \chi\delta^2\int_\Omega \nabla\bar{\mathbf{u}}\cdot\nabla\mathbf{u}\,dx\,dt\Big\}. \tag{11}$$

Note that $|\Omega|$ denotes the d-dimensional volume of the domain Ω and that the above analysis of the energy balance in the TRM holds for either $d = 2$ and 3. We further remark that setting either $\chi = 0$ or $\delta = 0$ reduces (11) to the usual rate of energy dissipation for the Navier–Stokes equations.

3.3. The Enstrophy Balance. Calculating enstrophy for TRM follows similar steps as for energy calculation except that our results only hold when $d = 2$ and the equation (1) is multiplied by the Laplacian of fluid velocity $\mathbf{u}$. Integrating over the domain Ω, one obtains

$$\begin{aligned}\int_\Omega \mathbf{u}_t\cdot\Delta\mathbf{u}\,dx + \int_\Omega (\mathbf{u}\cdot\nabla)\mathbf{u}\cdot\Delta\mathbf{u}\,dx - \nu\int_\Omega \Delta\mathbf{u}\cdot\Delta\mathbf{u}\,dx \\ + \int_\Omega \nabla p\cdot\Delta\mathbf{u}\,dx + \int_\Omega \chi(\mathbf{u}-\bar{\mathbf{u}})\cdot\Delta\mathbf{u}\,dx = 0.\end{aligned} \tag{12}$$

Integration by parts along with $\nabla\cdot\mathbf{u} = 0$ and the fact that we are now working only in the two-dimensional case gives us the following results

$$\int_\Omega \mathbf{u}_t\cdot\Delta\mathbf{u}\,dx = -\int_\Omega \nabla\times\mathbf{u}_t\cdot\nabla\times\mathbf{u}\,dx = -\frac{1}{2}\frac{d}{dt}\|\nabla\times\mathbf{u}\|^2,$$

$$\int_\Omega (\mathbf{u}\cdot\nabla)\mathbf{u}\cdot\Delta\mathbf{u}\,dx = 0 \qquad \text{and} \qquad \int_\Omega \nabla p\cdot\Delta\mathbf{u}\,dx = 0.$$

While the above orthogonality in the non-linear term only holds true in the periodic case, similar results could be obtained for two-dimensional flows in a smooth domain Ω with Dirichlet boundary conditions using the vorticity formulation after taking into account sources of enstrophy at the boundary. Thus, the equation (12) can be rewritten as

$$-\frac{1}{2}\frac{d}{dt}\|\nabla\times\mathbf{u}\|^2 - \nu\|\Delta\mathbf{u}\|^2 + \chi\int_\Omega (\mathbf{u}-\bar{\mathbf{u}})\cdot\Delta\mathbf{u}\,dx = 0. \tag{13}$$

Integrating (13) with respect to time yields

$$-\frac{1}{2}\|\nabla\times\mathbf{u}(T)\|^2 - \int_0^T \nu\|\Delta\mathbf{u}\|^2 dt + \int_0^T \chi\int_\Omega (\mathbf{u}-\bar{\mathbf{u}})\cdot\Delta\mathbf{u}\,dx\,dt = -\frac{1}{2}\|\nabla\times\mathbf{u}(0)\|^2. \tag{14}$$

Lemma 3.2. *Given* $\mathbf{u}$ *and* $\bar{\mathbf{u}}$ *are solutions to the TRM with the corresponding model parameters* χ *and* δ*, then* $\int_\Omega (\mathbf{u}-\bar{\mathbf{u}})\cdot\Delta\mathbf{u}\,dx \le 0$.

Proof. Based on the filtering equation (2) we have

$$\int_\Omega (\mathbf{u}-\bar{\mathbf{u}})\cdot\Delta\mathbf{u}\,dx = \int_\Omega -\delta^2\Delta\bar{\mathbf{u}}\cdot\Delta\mathbf{u}\,dx = \int_\Omega -\delta^2\Delta\bar{\mathbf{u}}\cdot\Delta(-\delta^2\Delta\bar{\mathbf{u}}+\bar{\mathbf{u}})\,dx.$$

Integration by parts yields

$$\int_\Omega (\mathbf{u}-\bar{\mathbf{u}})\cdot\Delta\mathbf{u}\,dx = -\delta^4\int_\Omega \|\nabla(\Delta\bar{\mathbf{u}})\|^2\,dx - \delta^2\int_\Omega \|\Delta\bar{\mathbf{u}}\|^2\,dx.$$

□

By the above lemma, equation (14) can be rewritten as

$$\frac{1}{2}\|\nabla\times\mathbf{u}(T)\|^2 + \int_0^T \nu\|\Delta\mathbf{u}\|^2 dt + \int_0^T \chi\delta^2\int_\Omega \Delta\bar{\mathbf{u}}\cdot\Delta\mathbf{u}\,dx\,dt = \frac{1}{2}\|\nabla\times\mathbf{u}(0)\|^2. \tag{15}$$

We define the TRM enhanced enstrophy dissipation rate, denoted by η, as follows

$$\eta = \frac{1}{T|\Omega|}\left\{\int_0^T \nu\|\Delta\mathbf{u}\|^2 dt + \int_0^T \chi\delta^2\int_\Omega \Delta\bar{\mathbf{u}}\cdot\Delta\mathbf{u}\,dx\,dt\right\}. \tag{16}$$

Remark 3.1. *The TRM energy and enstrophy dissipation rates in (11) and (16) each differ from the corresponding dissipation rates in the NSE only by one term.*

Remark 3.2. *Lemma 3.1 and Lemma 3.2 show that extra terms in rate of dissipation for TRM energy, ϵ, and enstrophy, η, are non-negative quantities. Thus, the TRM includes more dissipation of energy and enstrophy compared to the NSE.*

Remark 3.3. *Both quantities $\int_0^T \chi\delta^2\int_\Omega \nabla\bar{\mathbf{u}}\cdot\nabla\mathbf{u}\,dx\,dt$ and $\int_0^T \chi\delta^2\int_\Omega \Delta\bar{\mathbf{u}}\cdot\Delta\mathbf{u}\,dx\,dt$ depend on the parameters χ and δ. Choosing those parameters such that $\chi\delta^2\to 0$ results in ϵ and η approaching the rates of dissipation for energy and enstrophy in the NSE.*

3.4. Dimensional Analysis. This section describes the dimensional analysis used to study the scaling of the energy spectrum in the inertial ranges of the TRM. While our analysis of the energy cascade applies in both dimensions $d = 2$ and 3, the corresponding treatment of the enstrophy cascade as in [18] is generally valid only for periodic domains with $d = 2$. Note, however, the existence of a localized enstrophy cascade in three-dimensional turbulent flows has been shown under the assumption of a 1/2-Hölder coherence condition on the direction of the vorticity [7]. While a similar treatment of the TRM is outside the scope of the present work, it is an interesting question whether the scalings we deduce from the enstrophy balance also apply when $d = 3$ to energy spectra suitably localized in time and space.

The basic dimensional analysis we perform follows from an observation attributed to the American engineer and scientist E. Buckingham (1914). Generally speaking, the *Buckingham Pi Theorem* states that physical laws are independent of the form of the units. Therefore, acceptable laws of physics are homogeneous in all dimensions. In particular, we assume throughout the following analysis that the fluid is undergoing turbulent motion which is both homogeneous and isotropic. The actual statement of the theorem [31] we provide here for reference as

Theorem 3.4. Buckingham Pi Theorem. *Let $q_1, q_2, \ldots, q_n$ be n dimensional variables that are physically relevant in a given problem and that are inter-related by an unknown dimensionally homogeneous set of equations. These can be expressed via a functional relationship of the form*

$$F(q_1, q_2, \ldots, q_n) = 0 \qquad \textit{or equivalently} \qquad q_1 = f(q_2, \ldots, q_n).$$

If m is the number of fundamental dimensions required to describe the n variables, then there will be m primary variables and the remaining $n-m$ variables can be expressed as $n-m$ dimensionless and independent quantities or 'Pi groups', $\Pi_1, \Pi_2, \ldots, \Pi_{n-m}$. The functional relationship can thus be reduced to the much more compact form:

$$\Phi(\Pi_1, \Pi_2, \ldots, \Pi_{n-m}) = 0 \qquad \textit{or equivalently} \qquad \Pi_1 = \phi(\Pi_2, \ldots, \Pi_{n-m}).$$

Next we apply the Buckingham Pi process to determine dimensionless groups from the variables in TRM energy and enstrophy. We assume that there are $m = 2$ dimensional quantities to consider, *i.e.*, length $[L]$ and time $[T]$. The problem of deducing the behavior of TRM energy and enstrophy spectra both involve $n = 5$ variables, in general denoted as $q_1, \ldots, q_5$. As stated by the Buckingham Pi Theorem, $n - m = 3$ dimensionless groups of Π_1, Π_2 and Π_3 can be derived in both energy and enstrophy spectrum calculations. Primarily, we follow the steps listed below.

- Write down the dimensions for all 5 variables $q_1, \ldots, q_5$.
- Select 2 of the variables—say q_1, and q_2. These are called the repeating variables, and will appear in all the terms. Note that none of the repeating variables can be dimensionless and no two repeating variables can have the same overall dimension.
- Select one other variable—say q_3. Some combination of q_1, q_2, and q_3 is dimensionless, and forms the first dimensionless group Π_1. We can find the combination by dimensional analysis by writing $\Pi_1 = q_1^a q_2^b q_3$ or $[\ ] = [q_1]^a [q_2]^b [q_3]$, since equating exponents of each of the dimensional quantities gives two independent linear equations in the unknowns a and b.
- Repeat this procedure with the repeating variables and the next variable, so use q_1, q_2 and q_4. Continue until no variables are left.
- Having worked out all the dimensionless groups, the relationship between the variables can be expressed as a relationship between the various groups. Typically we write this as one group, *e.g.*, $\Pi_1 = \phi(\Pi_2, \Pi_3)$.

3.5. The Energy Cascade. Define the averaged energy spectrum over $[0, T]$ as

$$E(\kappa) = \frac{1}{2T\lambda_1^{1/2}} \int_0^T \sum_{k \in \mathcal{J}_\kappa} |\hat{u}_k|^2 dt \qquad \text{where} \qquad \mathbf{u} = \sum_{k \neq 0} \hat{u}_k e^{ik\cdot x}.$$

Here, due to the 2π periodicity, we have $\mathcal{J}_\kappa = \{\, k \in \mathbf{Z}^3 : \kappa - 1/2 < |k| \leq \kappa + 1/2 \,\}$. Thus, the average kinetic energy per unit volume is

$$\frac{1}{T|\Omega|} \int_0^T K(t) dt = \frac{1}{T|\Omega|} \int_0^T \frac{1}{2} \|\mathbf{u}\|^2 dt = \frac{1}{2T} \int_0^T \sum_{k \neq 0} |\hat{u}_k|^2 dt = \int_0^\infty E(\kappa) d\kappa.$$

The following table lists each variable in terms of its dimension based on the two-dimensional LT system, *i.e.*, length and time.

q_i	Description	Dimensions
ϵ	Energy dissipation rate	L^2T^{-3}
κ	Wave number	L^{-1}
E	Energy spectrum	L^3T^{-2}
δ	Filter length	L
χ	Time relaxation parameter	T^{-1}

Selecting the time averaged energy dissipation rate ϵ and the wave number κ as the repeating variables, our set up for the dimensionless groups is as follows.

$$\Pi_1 = \epsilon^a \kappa^b E \qquad \text{or} \qquad [\,] = [L^2T^{-3}]^a[L^{-1}]^b[L^3T^{-2}]$$
$$\Pi_2 = \epsilon^a \kappa^b \delta \qquad \text{or} \qquad [\,] = [L^2T^{-3}]^a[L^{-1}]^b[L]$$
$$\Pi_3 = \epsilon^a \kappa^b \chi \qquad \text{or} \qquad [\,] = [L^2T^{-3}]^a[L^{-1}]^b[T^{-1}]$$

Equating the coefficients leads us to the dimensionless groups of

$$\Pi_1 = \epsilon^{-2/3}\kappa^{5/3}E, \qquad \Pi_2 = \kappa\delta \qquad \text{and} \qquad \Pi_3 = \epsilon^{-1/3}\kappa^{-2/3}\chi.$$

Expressing Π_1 as a function of Π_2 and Π_3 yields

$$E(\kappa) = \epsilon^{2/3}\kappa^{-5/3}\phi(\kappa\delta, \epsilon^{-1/3}\kappa^{-2/3}\chi).$$

3.6. The Enstrophy Cascade. When $d = 2$ the enstrophy in the TRM is conserved by the non-linear term. Since the enstrophy spectrum is approximately $\kappa^2 E(\kappa)$ we perform our analysis in terms of the energy spectrum. Thus, the physical variables and their dimensions are as follows.

q_i	Description	Dimensions
η	Enstrophy dissipation rate	T^{-3}
κ	Wave number	L^{-1}
E	Energy spectrum	L^3T^{-2}
δ	Filter length	L
χ	Time relaxation parameter	T^{-1}

We choose the time averaged enstrophy dissipation rate η and the wave number κ as the repeating variables. Thus, the dimensionless groups are

$$\Pi_1 = \eta^a \kappa^b E \qquad \text{or} \qquad [\,] = [T^{-3}]^a[L^{-1}]^b[L^3T^{-2}]$$
$$\Pi_2 = \eta^a \kappa^b \delta \qquad \text{or} \qquad [\,] = [T^{-3}]^a[L^{-1}]^b[L]$$
$$\Pi_3 = \eta^a \kappa^b \chi \qquad \text{or} \qquad [\,] = [T^{-3}]^a[L^{-1}]^b[T^{-1}]$$

Solving for a and b in above equations gives us

$$\Pi_1 = \eta^{-2/3}\kappa^3 E, \qquad \Pi_2 = \kappa\delta \qquad \text{and} \qquad \Pi_3 = \eta^{-1/3}\chi.$$

Since Π_1 is a function of Π_2 and Π_3, then based on enstrophy balance, the two-dimensional TRM may also have an inertial range whose energy spectrum scales as

$$E(\kappa) = \eta^{2/3}\kappa^{-3}\phi(\kappa\delta, \eta^{1/3}\chi).$$

3.7. Computation of the Energy Spectrum. This section uses a spectral-Galerkin method to compute the energy spectrum of the TRM using a complicated time-dependent three-dimensional flow driven by a time-independent body force $\mathbf{f}$ that is 2π periodic in space. Under such a force, taking an initial condition $\mathbf{u}_0$ that is also 2π periodic in space leads to a solution $\mathbf{u}(x,t)$ that remains 2π periodic for all $t > t_0$. In our numerical simulations, we set $\nu = 0.0001$, choose $\mathbf{u}_0 = 0$ and take

$$\mathbf{f}(x) = \sum_{k\in\mathcal{J}} \mathbf{f}_k e^{ik\cdot x} \qquad \text{where} \qquad \mathcal{J} = \{\, k \in \mathbf{Z}^3 : 0 < |k| < 2 \,\}.$$

The numerical values of $\mathbf{f}_k$ used in our computations are given in Appendix A. The corresponding Grashof number $\mathcal{G}$ is

$$\mathcal{G} = \frac{\|\mathbf{f}\|_{L^2(\Omega)}}{\nu^2\lambda_1^{3/4}} = \frac{0.005}{(0.0001)^2} = 5 \times 10^5.$$

Here $\Omega = [0, 2\pi]^3$ and $\lambda_1 = 4\pi^2/L^2 = 1$ is the smallest eigenvalue of the Laplacian. Note that the exact initial condition $\mathbf{u}_0$ is inconsequential to this study, because our simulation will be run for a period of time long enough to forget the initial condition and enter into a time-dependent but statistically-steady flow that reflects only the energetics of the forcing.

As already mentioned in Section 3.1, the TRM contains no higher-order terms that obviously provide for the theoretical existence of strong solutions. While the question concerning regularity and the possible non-uniqueness of weak solutions is an interesting one, numerically we restrict our attention to finite collections of ordinary differential equations—the semi-discrete approximations of the TRM—which are clearly well posed. Our numerical solutions were obtained using a pseudo-spectral Galerkin method on a 512^3 grid dealiased according to the 2/3 rule. Thus, only modes such that

$$|k|_\infty = \max\{|k_1|, |k_2|, |k_3|\} \leq \left\lfloor \tfrac{2}{3} \cdot 256 \right\rfloor = 170$$

are used in our calculation. The corresponding Galerkin truncation of (5) represents a spatial discretization of the TRM which we integrate in time using the first-order exponential time-differencing scheme described by Cox and Matthews in [6] given by

$$\mathbf{u}_k^{n+1} = \exp(-L_k \Delta t)\mathbf{u}_k^n + \frac{\mathbf{f}_k - B(\mathbf{u}^n)_k}{L_k/2} \exp(-L_k \Delta t/2) \sinh(L_k \Delta t/2).$$

Here u_k^n is the approximation $u_k^n \approx u_k(t_n)$ for $t_n = t_0 + n\Delta t$ where Δt is the size of the time steps. Note this method is exact in the linear term and first-order in the convective term. Correctness of our computer code was verified by reproducing Figure 1a in Yang and Pullin [32].

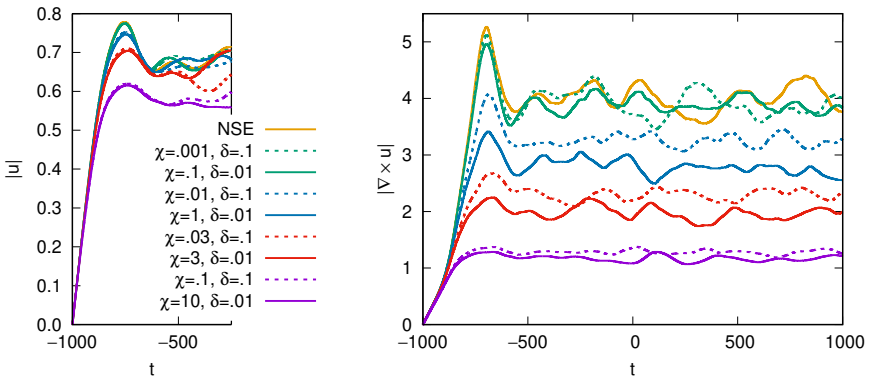

FIGURE 2. Time evolutions of the energy and the enstrophy norms for spatially periodic flows with $u_0 = 0$ when $t_0 = -1000$ given by the TRM method compared to a direct numerical simulation of the incompressible three-dimensional Navier–Stokes equations.

Computations were performed with $\Delta t = 0.001$ starting at $u_0 = 0$ when $t_0 = -1000$ and run until $T = 1000$ using the same parameter choices considered in Figure 1, namely χ and δ such that

$$\chi\delta^2 \in \{\, 10^{-5},\, 10^{-4},\, 3 \times 10^{-4},\, 10^{-3} \,\} \qquad \text{and} \qquad \delta \in \{\, 0.1,\, 0.01 \,\}.$$

We further include a direct numerical simulation of the incompressible three-dimensional Navier–Stokes equations. For reference the Reynolds number of the NSE flow reached

$$\mathrm{Re} = \frac{\|\mathbf{u}\|_{L^\infty}}{\lambda_1^{1/2}\nu} \approx 1{,}000 \qquad \text{by} \qquad t = 0$$

and fluctuated around that level for the remainder of the run. Figure 2 shows how the energy and enstrophy norms $\|\mathbf{u}\|$ and $\|\nabla \times \mathbf{u}\|$ evolve over time for the different values of χ and δ. Note again that trajectories corresponding to a choice parameters for which the values of $\chi\delta^2$ are equal have been depicted as solid and dotted lines of the same color.

Except for the strongest filters when $\chi\delta^2 = 10^{-3}$, the value of $\|\mathbf{u}\|$ reaches about 0.7 after 500 units of time have passed and continue to fluctuates around that level in a time-dependent manner into the future. Although the flows corresponding to strongest filters fail to express the same level of energetics, all flows exhibit complex time-dependent behavior. Note for each choice of parameters that $\|\nabla \times \mathbf{u}\|$ takes about the same time to reach an equilibrium level after which it also fluctuates around an average value. Although the average enstrophy resulting from the weakest filters when $\chi\delta^2 = 10^{-5}$ agrees roughly with the NSE, the enstrophy levels of the TRM, in general, depend strongly on the choice of χ and δ.

Having seen for every choice of the parameters χ and δ that the time-dependent flows starting at $u_0 = 0$ when $t_0 = -1000$ appear to reach a state by $t = 0$ in which their statistics are stationary, we compute the RMS time averages

$$\langle\|\mathbf{u}\|^2\rangle^{1/2} = \left(\frac{1}{T}\int_0^T \|\mathbf{u}\|^2 dt\right)^{1/2} \quad \text{and} \quad \langle\|\nabla \times \mathbf{u}\|^2\rangle^{1/2} = \left(\frac{1}{T}\int_0^T \|\nabla \times \mathbf{u}\|^2 dt\right)^{1/2},$$

where $T = 1000$ of the energy and enstrophy norms as well as the average rate of energy dissipation ϵ given by (11) and the dissipation wavenumber $\kappa_d = (\epsilon/\nu^3)^{1/4}$. We then examine the corresponding time-averaged energy spectra.

TABLE 1. The RMS averages of $\|\mathbf{u}\|_{L^2}$ and $\|\nabla \times \mathbf{u}\|_{L^2}$ over the interval $[0, T]$ where $T = 1000$ for the TRM using different values of χ and δ along with the corresponding average rate of dissipation of energy ϵ and the dissipation wavenumber $\kappa_d = (\epsilon/\nu^3)^{1/4}$.

χ	δ	$\langle\|\mathbf{u}\|^2\rangle^{1/2}$	$\langle\|\nabla \times \mathbf{u}\|^2\rangle^{1/2}$	ϵ	κ_d
0 (NSE)	0	0.671135	3.99276	6.42699×10^{-6}	50.3503
0.001	0.1	0.669031	3.84467	6.21124×10^{-6}	49.9223
0.1	0.01	0.676526	3.88167	6.66214×10^{-6}	50.8046
0.01	0.1	0.666761	3.24648	6.34408×10^{-6}	50.1871
1	0.01	0.650439	2.72843	5.96247×10^{-6}	49.4147
0.03	0.1	0.644672	2.30718	6.31150×10^{-6}	50.1226
3	0.01	0.639193	1.94382	6.07097×10^{-6}	49.6380
0.1	0.1	0.589612	1.28336	6.48723×10^{-6}	50.4678
10	0.01	0.576510	1.16471	6.00913×10^{-6}	49.5111

Table 1 confirms the observations about energy and enstrophy levels already gathered from Figure 2 while indicating, even though the enstrophy levels of the TRM depend quite strongly on χ and δ, that the average rates of energy dissipation ϵ and dissipation wave numbers κ_d do not. Although this might appear surprising, the result is quite natural and reflects the fact that the amount of energy produced

by the body force $\mathbf{f}$ is essentially the same in all cases. In particular, after an equilibrium is reached in which the energy dissipated is roughly equal to the energy added, it is reasonable for ϵ to depend on the force but not strongly on χ or δ.

Figure 3 illustrates the energy spectra averaged over the interval $[0, T]$ where $T = 1000$ for each of the flows already discussed. Since the body force $\mathbf{f}$ is supported on only the lowest modes in Fourier space, the modes $\mathbf{u}_k$ for $|k| \geq 2$ should reflect the spectral scaling found by dimensional analysis in Section 3.5. Note that the spectrum of the NSE decays to 10^{-13} by the 2/3 anti-aliasing cutoff, which is nearly zero; however, except for the weakest filter when $\chi\delta^2 = 10^{-5}$ each of the TRM methods result in a more compact spectrum which decays below 10^{-16} before the cutoff.

We remark the $|k|^{-5/3}$ inertial range of the NSE becomes more abbreviated in the time relaxation models as χ and δ increase and essentially disappears when $\chi\delta^2 = 10^{-3}$. Thus, increasing χ and δ leads to more compact energy spectra with diminished small scales. On the other hand, it is notable the energy which has accumulated in the low modes is comparable for each of the spectra in Figure 3. Since the low modes have not been forced to any particular energy level (as sometimes done, *e.g.*, see [5, 30]), the fact that those modes have similar energy levels for all choices of χ and δ suggests the modified cascade of energy of the TRM leaves invariant the rate at which energy transfers from the forcing range into the inertial range, even for the strongest filter. Consequently, the TRM appears to posses two properties important for a good turbulence model: an ability to reproduce the energetics of the large scales accurately while filtering the small scales. The next section explores from a practical point of view the extent to which the TRM allows for the efficient approximation of high Reynolds number flows using a course spatial discretization.

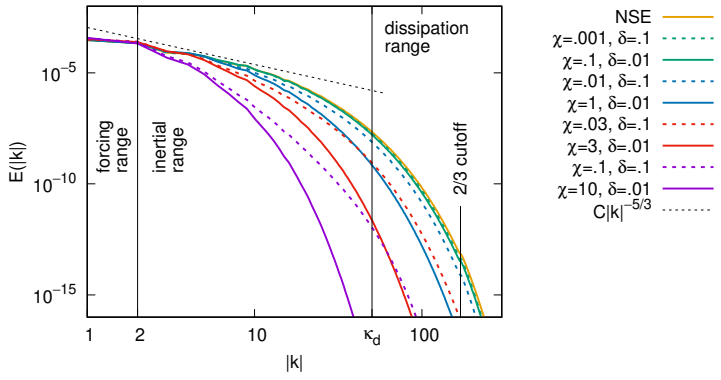

FIGURE 3. Average energy spectra over $[0, T]$ with $T = 1000$ of the TRM method compared to the incompressible three-dimensional Navier–Stokes equations. Indicated by κ_d is the Kolmogorov dissipation wavenumber corresponding to the NSE.

4. Finite-Element Computations

This section explores the use of the TRM in the finite-element codes commonly used to solve practical problems in computational fluid dynamics. We begin with the variational formulation needed to specify the computational algorithm and proceed to show that the resulting time-relaxation Oseen problem can be solved by a

globally convergence fixed-point iteration. While the proofs provided in Sections 4.1 and 4.2 assume Dirichlet boundary conditions, we note that similar results may also be obtained without difficulty in the case of periodic boundary conditions.

In Section 4.3 we perform a number of finite-element computations for the TRM using the Taylor–Green vortex as a benchmark problem. Since the resulting flow assumes periodic boundary conditions these computations could be done using spectral methods. However, the focus in this section—and indeed one of the main focuses of this paper—is the numerical implementation and performance of the TRM for finite-element computations. To this end, Section 4.3.1 checks the evolution of energy and enstrophy with respect to coarser meshes compared to a finer mesh Our work finishes with Section 4.3.2 in which the continuous sensitivity equations are computed to clarify how to tune δ and χ.

4.1. Variational Formulation and the Computational Algorithm. In this section we present the variational formulation and describe the finite-element computational algorithm used to solve the TRM. First, write equations (1) and (2) in variational form using a suitable choice of test functions from $\mathbf{X}$ and Q as

$$(\mathbf{u}_t, \mathbf{v}) + \nu a(\mathbf{u}, \mathbf{v}) + \ b^*(\mathbf{u}, \mathbf{u}, \mathbf{v}) - (p, \nabla \cdot \mathbf{v}) + \chi(\mathbf{u} - \bar{\mathbf{u}}, \mathbf{v}) = (\mathbf{f}, \mathbf{v}), \quad \forall \mathbf{v} \in \mathbf{X}, \tag{17}$$

$$(\nabla \cdot \mathbf{u}, q) = 0, \quad \forall q \in Q, \tag{18}$$

$$\delta^2(\nabla \bar{\mathbf{u}}, \nabla \mathbf{v}) + (\bar{\mathbf{u}}, \mathbf{v}) = (\mathbf{u}, \mathbf{v}), \quad \forall \mathbf{v} \in \mathbf{X}. \tag{19}$$

The numerical scheme used to solve the TRM is based on the continuous finite elements of [3]. In particular, we consider velocity and pressure finite-element spaces

$$\mathbf{X}^h \subset \mathbf{X} \qquad \text{and} \qquad Q^h \subset Q$$

and further define the space of discretely divergence-free velocity fields as

$$\mathbf{V}^h \ = \ \left\{ \mathbf{v} \in \mathbf{X}^h : (q, \nabla \cdot \mathbf{v}) = 0 \text{ for all } q \in Q^h \right\}.$$

Note that the velocity and pressure are assumed to satisfy the discrete inf-sup condition.

The method of Crank–Nicolson is used in time discretization of (17)-(19). Our notations in the time discretization equations of TRM read as $v(t^{n+1/2}) = v((t^{n+1} + t^n)/2)$ for the continuous variable and $v^{n+1/2} = (v^{n+1} + v^n)/2$ for both, continuous and discrete variables. Thus, the fully discretized finite element variational formulations of TRM are written as follows:

Given $(\mathbf{X}^h, Q^h)$, the time interval $[0, T]$ and a time step chosen such that $\Delta t < T = M\Delta t$, find the approximated TRM solution $(\mathbf{u}_h^{n+1}, p_h^{n+1}) \in (\mathbf{X}^h, Q^h)$, for $n = 0, 1, 2, \ldots, M-1$, satisfying

$$\frac{1}{\Delta t}(\mathbf{u}_h^{n+1} - \mathbf{u}_h^n, \mathbf{v}_h) + \nu a(\mathbf{u}_h^{n+1/2}, \mathbf{v}_h) + \ b^*(\mathbf{u}_h^{n+1/2}, \mathbf{u}_h^{n+1/2}, \mathbf{v}_h) - (p_h^{n+1}, \nabla \cdot \mathbf{v}_h)$$
$$+\chi(\mathbf{u}_h^{n+1/2} - \bar{\mathbf{u}}_h^{n+1/2}, \mathbf{v}_h) = (\mathbf{f}^{n+1/2}, \mathbf{v}_h), \quad \forall \mathbf{v}_h \in \mathbf{X}^h, \tag{20}$$

$$(\nabla \cdot \mathbf{u}_h^{n+1}, q_h) = 0, \quad \forall q_h \in Q^h, \tag{21}$$

$$\delta^2(\nabla \bar{\mathbf{u}}_h^{n+1}, \nabla \mathbf{v}_h) + (\bar{\mathbf{u}}_h^{n+1}, \mathbf{v}_h) = (\mathbf{u}_h^{n+1}, \mathbf{v}_h), \quad \forall \mathbf{v}_h \in \mathbf{X}^h. \tag{22}$$

In the space $\mathbf{V}^h$, equations (20) through (22) may equivalently be rewritten as follows: Find $\mathbf{u}_h^{n+1} \in \mathbf{V}^h$, for $n = 0, 1, 2, \ldots, M-1$, satisfying

$$\frac{1}{\Delta t}(\mathbf{u}_h^{n+1} - \mathbf{u}_h^n, \mathbf{v}_h) + \nu a(\mathbf{u}_h^{n+1/2}, \mathbf{v}_h) + \ b^*(\mathbf{u}_h^{n+1/2}, \mathbf{u}_h^{n+1/2}, \mathbf{v}_h)$$

$$+\chi(\mathbf{u}_h^{n+1/2} - \bar{\mathbf{u}}_h^{n+1/2}, \mathbf{v}_h) = (\mathbf{f}^{n+1/2}, \mathbf{v}_h), \quad \forall \mathbf{v}_h \in \mathbf{V}^h, \tag{23}$$

$$\delta^2(\nabla \bar{\mathbf{u}}_h^{n+1}, \nabla \mathbf{v}_h) + (\bar{\mathbf{u}}_h^{n+1}, \mathbf{v}_h) = (\mathbf{u}_h^{n+1}, \mathbf{v}_h), \quad \forall \mathbf{v}_h \in \mathbf{V}^h. \tag{24}$$

In our computations, the non-linear term $b^*(\mathbf{u}_h^{n+1/2}, \mathbf{u}_h^{n+1/2}, \mathbf{v}_h)$ in equation (23) is approximated by the method of fixed point iteration. This leads us to solve an Oseen type of equation repeatedly at any single time step. In the following section, we introduce the governing TRM Oseen equations and prove the uniqueness and existence of the solution. In addition, we show that the calculated sequence of fixed points is globally convergent.

4.2. The Time Relaxation Oseen Problem. In the process of linearizing the TRM equations given in the previous section, we end up solving equations similar to Oseen problem for Navier-Stokes equations introduced in [20] at any single time level. Here we provide a detailed analysis of the solution to this type of equations referred as the Time Relaxation Oseen problem, TRO, following work done for NSE from [20]. Since the analysis of the discrete case is analogous to that for the continuous problem, this section covers only the results in continuous case.

Given a divergence-free vector field $\mathbf{b}$ that vanishes on $\partial\Omega$, and is smooth enough, the TRO problem is to find $(\mathbf{u}, p)$ satisfying:

$$-\nu\Delta\mathbf{u} + \mathbf{b}\cdot\nabla\mathbf{u} + \nabla p + \chi(\mathbf{u} - \bar{\mathbf{u}}) = \mathbf{f}, \tag{25}$$

$$\nabla \cdot \mathbf{u} = 0, \tag{26}$$

$$-\delta^2\Delta\bar{\mathbf{u}} + \bar{\mathbf{u}} = \mathbf{u}, \tag{27}$$

where in addition, $\mathbf{u}$ is zero on $\partial\Omega$ and $\int_\Omega p\, dx = 0$.

Next, we derive the variational formulation of TRO in the space of divergence-free functions $\mathbf{V}$. Let $A(\mathbf{u}, \mathbf{v}) = \nu(\nabla\mathbf{u}, \nabla\mathbf{v}) + (\mathbf{b}\cdot\nabla\mathbf{u}, \mathbf{v}) + \chi(\mathbf{u} - \bar{\mathbf{u}}, \mathbf{v})$. Then, the problem is to find $\mathbf{u} \in \mathbf{V}$ such that:

$$A(\mathbf{u}, \mathbf{v}) = (\mathbf{f}, \mathbf{v}), \tag{28}$$

$$\delta^2(\nabla\bar{\mathbf{u}}, \nabla\mathbf{v}) + (\bar{\mathbf{u}}, \mathbf{v}) = (\mathbf{u}, \mathbf{v}). \tag{29}$$

Lemma 4.1. *Given a vector field $\mathbf{b} \in \mathbf{V}$, the operator $A(\cdot,\cdot)$ is coercive and continuous, i.e.,*

$$A(\mathbf{u}, \mathbf{u}) \geq \nu\|\nabla\mathbf{u}\|^2, \quad \forall \mathbf{u} \in \mathbf{V},$$
$$A(\mathbf{u}, \mathbf{v}) \leq (\nu + C_1\|\nabla\mathbf{b}\| + C_2\chi)\|\nabla\mathbf{u}\|\|\nabla\mathbf{v}\|, \quad \forall \mathbf{u}, \mathbf{v} \in \mathbf{V}.$$

Proof. By definition of $A(\cdot,\cdot)$, we have

$$A(\mathbf{u}, \mathbf{u}) = \nu\|\nabla\mathbf{u}\|^2 + \chi\|\mathbf{u}\|^2 - \chi(\bar{\mathbf{u}}, \mathbf{u}). \tag{30}$$

Cauchy-Schwarz along with Lemma 2.2 yields

$$(\bar{\mathbf{u}}, \mathbf{u}) \leq \|\mathbf{u}\|^2. \tag{31}$$

Coercivity of the operator $A(\cdot,\cdot)$ is an immediate result of using the inequality (31) in (30).

Applying the Cauchy–Schwarz inequality and Lemma 2.1 to the definition of $A(\cdot,\cdot)$, one obtains

$$A(\mathbf{u},\mathbf{v}) \leq (\nu + C_1(\Omega)\|\nabla \mathbf{b}\|)\|\nabla \mathbf{u}\|\|\nabla \mathbf{v}\| + \chi\|\mathbf{u}-\bar{\mathbf{u}}\|\|\mathbf{v}\|. \tag{32}$$

The continuity is obtained by bounding the last term of (32) on the right-hand side using the Poincaré inequality and Lemma 2.2 as following

$$\|\mathbf{u}-\bar{\mathbf{u}}\|\|\mathbf{v}\| \leq (\|\mathbf{u}\| + \|\bar{\mathbf{u}}\|)\|\mathbf{v}\| \leq 2C_{PF}^2\|\nabla \mathbf{u}\|\|\nabla \mathbf{v}\|. \tag{33}$$

□

Corollary 4.1. *For any vector field* $\mathbf{b} \in \mathbf{V}$ *the Time Relaxation Oseen problem has a unique solution* $\mathbf{u} \in \mathbf{V}$ *given* $\mathbf{f} \in \mathbf{X}^*$ *is fixed. In addition, the solution* $\mathbf{u}$ *satisfies*

$$\nu\|\nabla \mathbf{u}\| \leq \|\mathbf{f}\|_*. \tag{34}$$

Proof. This follows from Lax–Milgram theorem defining $F(\mathbf{v}) = (\mathbf{f},\mathbf{v})$. □

Definition 4.1. *Let* $\mathbf{b}$ *be the vector field and* $\mathbf{u}$ *be the solution of the TRO given by equations (4.1) through (27), then* $T\colon \mathbf{V} \to \mathbf{V}$ *is defined as* $T(\mathbf{b}) = \mathbf{u}$.

One can notice that a fixed point of T is a vector $\mathbf{u}^* \in \mathbf{V}$ such that $T(\mathbf{u}^*) = \mathbf{u}^*$ and it satisfies the steady TRM in (1).

Lemma 4.2. *The map* $T\colon \mathbf{V} \to \mathbf{V}$ *in Definition 4.1 is a global contraction under the following assumptions:*

$$\frac{C(\Omega)}{\nu(\nu - C_{PF}^2\chi)}\|\mathbf{f}\|_* < 1 \text{ and } \nu > C_{PF}^2\chi,$$

for constants $C(\Omega)$ *and* C_{PF}.

Proof. Let $T(\mathbf{b}_1) = \mathbf{u}_1$ and $T(\mathbf{b}_2) = \mathbf{u}_2$, we show that $\|T(\mathbf{b}_1) - T(\mathbf{b}_2)\|_{\mathbf{X}} \leq \beta\|\mathbf{b}_1 - \mathbf{b}_2\|_{\mathbf{X}}$ for $\beta < 1$. Following the definition of T, we have

$$\nu(\nabla \mathbf{u}_1, \nabla \mathbf{v}) + (\mathbf{b}_1 \cdot \nabla \mathbf{u}_1, \mathbf{v}) + \chi(\mathbf{u}_1 - \bar{\mathbf{u}}_1, \mathbf{v}) = (\mathbf{f},\mathbf{v}), \tag{35}$$

$$\nu(\nabla \mathbf{u}_2, \nabla \mathbf{v}) + (\mathbf{b}_2 \cdot \nabla \mathbf{u}_2, \mathbf{v}) + \chi(\mathbf{u}_2 - \bar{\mathbf{u}}_2, \mathbf{v}) = (\mathbf{f},\mathbf{v}). \tag{36}$$

Subtracting the two equations (35) and (36), and using the notation $\phi = \mathbf{u}_1 - \mathbf{u}_2$, the following equation is obtained

$$\nu(\nabla \phi, \nabla \mathbf{v}) + (\mathbf{b}_1 \cdot \nabla \mathbf{u}_1 - \mathbf{b}_2 \cdot \nabla \mathbf{u}_2, \mathbf{v}) + \chi(\phi - \bar{\phi}, \mathbf{v}) = 0. \tag{37}$$

In (37), the term $\mathbf{b}_1 \cdot \nabla \mathbf{u}_1 - \mathbf{b}_2 \cdot \nabla \mathbf{u}_2$ can be modified as $\mathbf{b}_1 \cdot \nabla \phi + (\mathbf{b}_1 - \mathbf{b}_2) \cdot \nabla \mathbf{u}_2$ by adding and subtracting $\mathbf{b}_1 \cdot \nabla \mathbf{u}_2$. When setting $\mathbf{v} = \phi$ and rearranging the terms, one obtains

$$\nu\|\nabla \phi\|^2 + \chi\|\phi\|^2 = -((\mathbf{b}_1 - \mathbf{b}_2) \cdot \nabla \mathbf{u}_2, \phi) + \chi(\bar{\phi}, \phi). \tag{38}$$

In the next step, we bound the terms on the right-hand side of (38). Lemma 2.1 and Corollary 4.1 provide a bound for the first term. The second term is bounded using the Cauchy–Schwarz and Poincaré inequalities followed by Lemma 2.2. Thus

$$\nu\|\nabla \phi\|^2 + \chi\|\phi\|^2 \leq C(\Omega)\nu^{-1}\|\mathbf{f}\|_*\|\nabla(\mathbf{b}_1 - \mathbf{b}_2)\|\|\nabla \phi\| + C_{PF}^2\chi\|\nabla \phi\|^2. \tag{39}$$

Rearranging the terms gives

$$(\nu - C_{PF}^2\chi)\|\nabla \phi\|^2 \leq C(\Omega)\nu^{-1}\|\mathbf{f}\|_*\|\nabla(\mathbf{b}_1 - \mathbf{b}_2)\|\|\nabla \phi\|, \tag{40}$$

i.e.

$$\|\nabla \phi\| \leq \frac{C(\Omega)}{\nu(\nu - C_{PF}^2\chi)}\|\mathbf{f}\|_*\|\nabla(\mathbf{b}_1 - \mathbf{b}_2)\|. \tag{41}$$

Take $\beta = \frac{C(\Omega)}{\nu(\nu - C_{PF}^2\chi)}\|\mathbf{f}\|_* < 1$ in (41), then

$$\|\nabla(\mathbf{u}_1 - \mathbf{u}_2)\| \leq \beta\|\nabla(\mathbf{b}_1 - \mathbf{b}_2)\|.$$

Thus T is a global contraction map. □

The next natural step is to show the existence of a solution to the steady TRM. In this paper, we provide this proof via showing that the generated sequence of fixed points is globally convergent. Given $\mathbf{u}^{(0)} \in \mathbf{V}$, we calculate $\mathbf{u}^{(1)}, \mathbf{u}^{(2)}, \mathbf{u}^{(3)}, \cdots \in \mathbf{V}$ in the following manner

$$\delta^2(\nabla\bar{\mathbf{u}}^{(k)}, \nabla\mathbf{v}) + (\bar{\mathbf{u}}^{(k)}, \mathbf{v}) = (\mathbf{u}^{(k)}, \mathbf{v}), \tag{42}$$

$$\nu(\nabla\mathbf{u}^{(k+1)}, \nabla\mathbf{v}) + (\mathbf{u}^{(k)} \cdot \nabla\mathbf{u}^{(k+1)}, \mathbf{v}) + \chi(\mathbf{u}^{(k+1)} - \bar{\mathbf{u}}^{(k)}, \mathbf{v}) = (\mathbf{f}, \mathbf{v}). \tag{43}$$

Note that by definition of T, we have $\mathbf{u}^{(k+1)} = T(\mathbf{u}^{(k)})$. To simplify the notation, we omit the parenthesis argument of T and denote the k-th iteration by T^k so that $\mathbf{u}^{(k)} = T^k\mathbf{u}^{(0)}$.

Theorem 4.2. *The sequence of fixed point iterations $\{\mathbf{u}^{(k)}\}_{k=0}^{\infty}$ forms a Cauchy sequence and converges to the unique solution of TRM, $\mathbf{u}$, as $k \to \infty$ provided*

$$\nu^{-2}(C(\Omega)\|\mathbf{f}\|_* + C_{PF}^2\nu\chi) < 1, \tag{44}$$

where $C(\Omega)$ and C_{PF} are constants.

Proof. First we show that $\{\mathbf{u}^{(k)}\}_{k=0}^{\infty}$ is a Cauchy sequence. If $\beta = \frac{C(\Omega)}{\nu(\nu - C_{PF}^2\chi)}\|\mathbf{f}\|_* < 1$ and $k \geq l \geq 1$, then from Lemma 4.2 and the triangle inequality, we have

$$\begin{aligned}
\|u^{(k)} - u^{(l)}\|_{\mathbf{X}} &= \|T^k u^{(0)} - T^l u^{(0)}\|_{\mathbf{X}} \leq \beta^l \|T^{k-l}u^{(0)} - u^{(0)}\|_{\mathbf{X}} \\
&\leq \beta^l \big[\|T^{k-l}u^{(0)} - T^{k-l-1}u^{(0)}\|_{\mathbf{X}} + \|T^{k-l-1}u^{(0)} - T^{k-l-2}u^{(0)}\|_{\mathbf{X}} \\
&\qquad + \cdots + \|Tu^{(0)} - u^{(0)}\|_{\mathbf{X}}\big] \\
&\leq \beta^l \Big(\sum_{j=0}^{k-l-1} \beta^j\Big)\|u^{(1)} - u^{(0)}\|_{\mathbf{X}} \leq \frac{\beta^l}{1-\beta}\|u^{(1)} - u^{(0)}\|_{\mathbf{X}}.
\end{aligned}$$

This simply implies that $\{\mathbf{u}^{(k)}\}_{k=0}^{\infty}$ is Cauchy. In the next step, we prove that the sequence of fixed point iterations converges towards the steady TRM solution.

Let $\mathbf{e}^k$ denote $\mathbf{u} - \mathbf{u}^{(k)}$. Since the filtering equation in TRO is linear, therefore $\bar{\mathbf{e}}^k = \bar{\mathbf{u}} - \bar{\mathbf{u}}^{(k)}$. Subtracting equation (43) from the corresponding steady TRM equation gives

$$\nu(\nabla\mathbf{e}^{k+1}, \nabla\mathbf{v}) + (\mathbf{u} \cdot \nabla\mathbf{u} - \mathbf{u}^{(k)} \cdot \nabla\mathbf{u}^{(k+1)}, \mathbf{v}) + \chi(\mathbf{e}^{k+1} - \bar{\mathbf{e}}^k, \mathbf{v}) = 0. \tag{45}$$

In the above equation, treat the second term from right-hand side $\mathbf{u} \cdot \nabla\mathbf{u} - \mathbf{u}^{(k)} \cdot \nabla\mathbf{u}^{(k+1)}$ as

$$\begin{aligned}
\mathbf{u} \cdot \nabla\mathbf{u} - \mathbf{u}^{(k)} \cdot \nabla\mathbf{u}^{(k+1)} &= \mathbf{u} \cdot \nabla\mathbf{u} - \mathbf{u}^{(k)} \cdot \nabla\mathbf{u} + \mathbf{u}^{(k)} \cdot \nabla\mathbf{u} - \mathbf{u}^{(k)} \cdot \nabla\mathbf{u}^{(k+1)} \\
&= \mathbf{e}^k \cdot \nabla\mathbf{u} - \mathbf{u}^{(k)} \cdot \nabla\mathbf{e}^{k+1}.
\end{aligned}$$

Thus (45) is rewritten as

$$\nu(\nabla\mathbf{e}^{k+1}, \nabla\mathbf{v}) + (\mathbf{e}^k \cdot \nabla\mathbf{u} - \mathbf{u}^{(k)} \cdot \nabla\mathbf{e}^{k+1}, \mathbf{v}) + \chi(\mathbf{e}^{k+1} - \bar{\mathbf{e}}^k, \mathbf{v}) = 0. \tag{46}$$

Setting $\mathbf{v} = \mathbf{e}^{k+1}$ in (46) and rearranging the terms, one obtains

$$\nu\|\nabla\mathbf{e}^{k+1}\|^2 + \chi\|\mathbf{e}^{k+1}\|^2 = -(\mathbf{e}^k \cdot \nabla\mathbf{u}, \mathbf{e}^{k+1}) + \chi(\bar{\mathbf{e}}^k, \mathbf{e}^{k+1}). \tag{47}$$

Applying Cauchy–Schwarz and Poincaré inequalities in addition to Lemma 2.1, Lemma 2.2 and Corollary 4.1 yields

$$\nu\|\nabla \mathbf{e}^{k+1}\|^2 + \chi\|\mathbf{e}^{k+1}\|^2 \leq (C(\Omega)\nu\|\mathbf{f}\|_* + C_{PF}^2\chi)\|\nabla \mathbf{e}^k\|\|\nabla \mathbf{e}^{k+1}\|. \tag{48}$$

Thus,

$$\nu\|\nabla \mathbf{e}^{k+1}\|^2 \leq (C(\Omega)\nu\|\mathbf{f}\|_* + C_{PF}^2\chi)\|\nabla \mathbf{e}^k\|\|\nabla \mathbf{e}^{k+1}\|, \tag{49}$$

or

$$\|\nabla \mathbf{e}^{k+1}\| \leq \nu^{-2}(C(\Omega)\|\mathbf{f}\|_* + C_{PF}^2\nu\chi)\|\nabla \mathbf{e}^k\|. \tag{50}$$

Given that $\nu^{-2}(C(\Omega)\|\mathbf{f}\|_* + C_{PF}^2\nu\chi) < \alpha < 1$, then using induction $\|\nabla \mathbf{e}^k\| < \alpha^k\|\nabla \mathbf{e}^0\|$ as $k \to \infty$, the convergence of fixed point iterations is concluded. □

Remark 4.3. *One observes that under the assumptions of Lemma 4.2, it is obvious that* $\frac{C(\Omega)}{\nu^2}\|\mathbf{f}\|_* < 1$. *Thus in Theorem 4.2, the convergence of the fixed point iteration is subject to choosing the model parameter* χ *such that* $C_{PF}^2\nu^{-1}\chi < 1 - \frac{C(\Omega)}{\nu^2}\|\mathbf{f}\|_*$.

4.3. Taylor–Green Vortex. The Taylor–Green vortex is an unsteady flow of a decaying vortex [2]. Specifically, it is a three-dimensional incompressible flow, that evolves from a two-dimensional velocity field [12], given by

$$\begin{aligned} u_1(x, y, z, 0) &= \sin x \cos y \cos z, \\ u_2(x, y, z, 0) &= -\cos x \sin y \cos z, \\ u_3(x, y, z, 0) &= 0, \end{aligned} \tag{51}$$

with periodic boundary conditions on $[0, 2\pi]^3$ as shown in [12, 10]. Figure 4b shows a two-dimensional slice of the velocity field shown in black with vorticity shown in red for the initial Taylor–Green vortex taken along the xy-plane at $z = 0$. We can see in Figure 4b that the vortices in the top left and bottom right of the xy-plane move in the counterclockwise direction, while the two vortices in the top right and bottom left move in the clockwise direction.

Let the initial density $\rho(\mathbf{x}, 0) = 1$ as in [10]. The initial kinetic energy is

$$K(0) = \frac{1}{2}\|\mathbf{u}(\cdot, 0)\|_{L^2(\Omega)}^2 = \frac{1}{4}\int_0^{2\pi}\int_0^{2\pi}\int_0^{2\pi} [1 - \cos(2x)\cos(2y)]\cos^2(z)\, dx\, dy\, dz = \pi^3,$$

for the corresponding Taylor–Green vortex. Therefore, the dissipation can be examined by observing the rate of decrease of the kinetic energy from its initial value π^3 over time [12, 10]. Note that the flow quickly develops a tightly twisted vortex core. As production of vorticity is proportional to the derivative of the velocity vector, there should be a growth in enstrophy, see [12]. This increase is also seen for the TRM in our simulation results. The vorticity is shown by Figure 4, with the vorticity vectors given in red.

4.3.1. TRM Energy and Enstrophy Performance. We study the effects of the time relaxation model for four mesh levels: a mesh level 1 consisting of 3,072 tetrahedral elements (or 8 subintervals in all three directions), a mesh level 2 consisting of 6,000 tetrahedral elements (or 10 subintervals in all three directions), a mesh level 3 consisting of 10,368 tetrahedral elements (or 12 subintervals in all three directions) and a fine mesh level 4 of 16,464 tetrahedral elements (or 14 subintervals in all three directions).

All finite-element calculations were performed with FreeFem++ [17]. Using (P_2, P_1) Taylor–Hood elements, we set our test functions for velocity to be piecewise quadratic equations and our test functions for pressure to be piecewise linear functions.

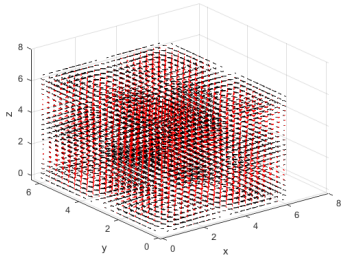

(A) The vorticity of the Taylor–Green vortex in three dimensions

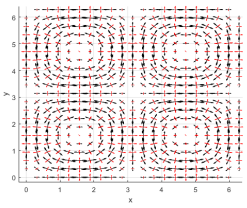

(B) The vorticity field of the Taylor–Green vortex, taken along the xy-plane at $z = 0$.

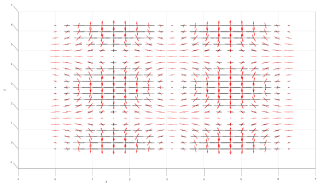

(C) The vorticity field of the Taylor–Green vortex, taken along the xz-plane at $y = 0$.

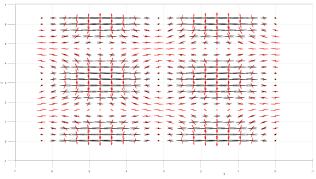

(D) The vorticity field of the Taylor–Green vortex, taken along the yz-plane at $x = 0$.

FIGURE 4. The vorticity (in red) and velocity (in black) fields of the Taylor–Green vortex.

Setting the size of the time step $\Delta t = 0.001$, the simulations ran on the time interval $[0, 0.1]$ corresponding to 100 times steps. We test the TRM at relaxation parameters $\chi = 0$ that is equivalent to the NSE, against our model using the stop criterion $\varepsilon = 1.0 \times 10^{-10}$ for the TRO fixed-point iteration defined in Section 4.

Note that the Reynolds number $\mathrm{Re} = 500{,}000$ of the Taylor–Green flow considered in this section is approximately 500 times greater than the Reynolds numbers of the flows used to compute the energy spectra in Section 3.7 while the finite-element simulations represent a much coarser spatial discretization. On the other hand, the initial condition (51) begins with no small-scale eddies and the interval of time over which our computation will be run is short enough that the energy cascade transports very little energy into the dissipation range. Therefore, we expect energy levels to remain essentially constant over the entire run. Moreover, even though the Reynolds number is high, since small scales do not play an important role in the early evolution of the Taylor–Green vortex, it should intuitively be possible to obtain reasonable approximations using a coarse mesh.

Figure 5 plots the normalized kinetic energy and enstrophy. We observe that the enstrophy increases as expected, and the normalized kinetic energy stays constant at near unity for the NSE and experiences a slightly greater dissipation for the chosen values of δ and χ in the TRM. For all choices of parameters, every solution trajectory has gained about a 0.7 percent increase in enstrophy by time $t = 0.1$ while experiencing less than 0.1 percent decrease in energy.

To better understand how the mesh interacts with the filtering properties of the TRM we further performed a resolution study ranging from 6,000 finite (tetrahedral) elements to using 68,388 finite (tetrahedral) elements for the same Taylor–Green initial conditions. The resulting evolutions in energy and enstrophy are

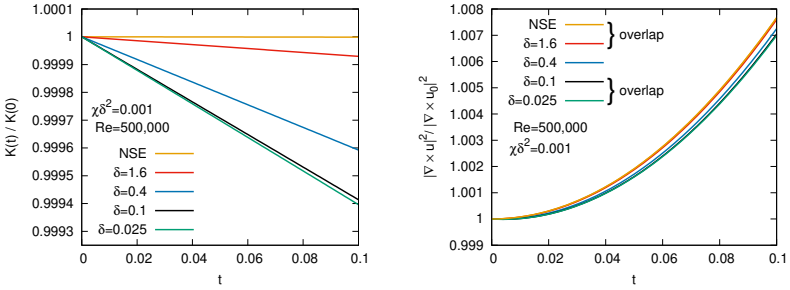

(A) Normalized kinetic energy (B) Normalized enstrophy

FIGURE 5. Energy and enstrophy versus time for Reynolds number Re = 500,000 computed using 6,000 tetrahedral elements for varying values of χ and δ such that $\chi\delta^2 = 0.001$.

provided in Figures 6a and 6b respectively. For comparison the same computation performed using the spectral method described in Section 3.7 has been included. It is interesting that on every mesh considered the TRM with parameters $\chi = 0.1$ and $\delta = 0.05$ performs similarly to the NSE computed on the same mesh.

Although the computed energy levels in Figure 6a visually agree for all the finite element meshes considered and are consistent with the spectral code, the evolution of the enstrophy in Figure 6b experiences a noticeable dependence on the resolution. While it is difficult to match the accuracy of a spectral calculation using a finite-element code, it should be observed from the scales in the graphs that the effects we are observing involve less than a percent difference in the actual physical values. In particular, the goal of a turbulence model as well most finite element calculations is not to reproduce an exact solution as much as to find an approximate solution that yields correct qualitative behavior. For example, even a 10 percent error may be acceptable in certain engineering problems and other applications.

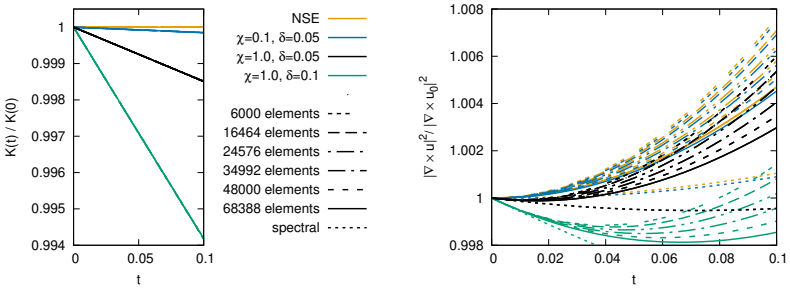

(A) Normalized kinetic energy (B) Normalized enstrophy

FIGURE 6. Energy and enstrophy versus time for Reynolds number Re = 500,000 for selected values of χ and δ at varying spatial resolutions.

We looked into the following statistics to evaluate the computational efficiency of the TRM. Let `itnlavg` denote the average number of iterations needed to solve the TRO at each time step and let `itnlmax` denote the maximum number of iterations needed to solve the TRO for the worst time step. Statistics for runs using 34, 992

finite elements taken over 100 time steps of size $\Delta t = 0.001$ are given in Table 2. We remark that the statistics in the Table 2 appear to indicate that the TRM has no advantage in terms of computational savings for any of the resolutions or model parameters chosen. This may be because small scale motion does not play a significant role in the early time evolution of the Taylor–Green vortex; however, further investigation would be needed to confirm this. Note that in no cases did the Oseen iterations for solving the NSE and TRM fail to converge.

TABLE 2. Data indicating the number of Oseen iterations used for nonlinear term taken over the first 100 time-steps with size $\Delta t = 0.001$ of the evolution of the Taylor–Green vortex. Here `itnlave` indicates the average number of Oseen iterations needed per time step and `itnlmax` indicates the maximum number needed for the worst time step.

elements	χ	δ	`itnlavg`	`itnlmax`
34992	0.00	0.10	7.38	18
34992	0.01	0.01	7.03	23
34992	0.10	0.05	7.49	19
34992	1.00	0.05	7.04	19
34992	1.00	0.10	6.96	18

4.3.2. TRM Parameter Sensitivity and Energy Dissipation. The TRM energy and enstrophy calculations in Section 4.3.1 show that the time evolution of both quantities depend on the model parameter values of χ and δ. The rate of energy dissipation ϵ given by (11) for the TRM and the rate of enstrophy dissipation η given by (16) in the two-dimensional case indicate that choosing the parameters χ and δ in such a way that $\chi\delta^2 \to 0$ is important since in that limit the enhancement to the dissipation in the TRM vanishes and ϵ and η approach the corresponding dissipation rates for the NSE.

Here we provide a numerical study of the energy dissipation in relation to the sensitivity of the model with respect to the variation of χ when using the TRM to compute the initial evolution of the Taylor–Green vortex. Parameter sensitivity analysis of the TRM with respect to χ using the continuous sensitivity equation method, CSEM, can be found in [25]. In particular, the sensitivity equations are obtained by differentiating the TRM equations (1) and (2) with respect to χ. Thus, given $(\mathbf{u}, p)$, we compute $(\mathbf{s}, r)$ subject to periodic boundary conditions such that

$$\begin{aligned} \mathbf{s}_t + \mathbf{u}\cdot\nabla\mathbf{s} + \mathbf{s}\cdot\nabla\mathbf{u} + \nabla r - \nu\Delta\mathbf{s} + (\mathbf{u}-\bar{\mathbf{u}}) + \chi(\mathbf{s}-\mathbf{w}) = 0 \quad &\text{in} \quad \Omega\times[0,T], \\ \nabla\cdot\mathbf{s} = 0 \quad &\text{in} \quad \Omega\times[0,T], \end{aligned} \tag{52}$$

where $\mathbf{s} = \partial\mathbf{u}/\partial\chi$, $r = \partial p/\partial\chi$ and $\mathbf{w} = \partial\bar{\mathbf{u}}/\partial\chi$. Here $\mathbf{w}$ satisfies the filtering equation

$$-\delta^2\Delta\mathbf{w} + \mathbf{w} \;=\; \mathbf{s} \quad \text{in} \quad \Omega \tag{53}$$

again subject to periodic boundary conditions. Since the initial condition (51) does not depend on χ, we take the initial condition of $\mathbf{s}$ at time $t = 0$ to be $\mathbf{s}_0 = 0$.

In this numerical experiment, the sensitivity equations (52) and (53) are treated using the method of Crank–Nicolson for time discretization and finite element for

discretization in space obtaining a numerical scheme as developed in [25]. As we see in (52), $\mathbf{u}$ appears in the sensitivity equation. Hence, in order to obtain the solution for (52) we need to couple (1) with (52). All the computations are carried out with a uniform time-step $\Delta t = 0.01$ using the Taylor–Hood finite elements on the time interval [0, 0.1]. The selected spatial mesh size consists of 10 subintervals in the x, y and z directions for a total of 6,000 elements.

TABLE 3. TRM energy dissipation and $\chi\|\mathbf{s}\|_{\ell^2(0,1;L^2(\Omega))}$ for $\delta = 0.1$.

χ	$\chi\delta^2$	$K(0) - K(t)$	$\chi\|\mathbf{s}\|_{\ell^2(0,1;L^2(\Omega))}$
0.01	10^{-4}	1.81368×10^{-4}	1.69108×10^{-3}
0.1	10^{-3}	1.81286×10^{-3}	1.68995×10^{-2}
1	10^{-2}	1.81139×10^{-2}	1.67876×10^{-1}
10	10^{-1}	1.79530×10^{-1}	1.57201

TABLE 4. TRM energy dissipation and $\chi\|\mathbf{s}\|_{\ell^2(0,1;L^2(\Omega))}$ for $\delta = 0.01$.

χ	$\chi\delta^2$	$K(0) - K(t)$	$\chi\|\mathbf{s}\|_{\ell^2(0,1;L^2(\Omega))}$
0.01	10^{-6}	1.94815×10^{-6}	1.74014×10^{-3}
0.1	10^{-5}	1.88145×10^{-5}	1.73935×10^{-2}
1	10^{-4}	1.88318×10^{-4}	1.73152×10^{-1}
10	10^{-3}	1.97178×10^{-3}	1.65695

We consider using sensitivity as an accuracy measure of the approximated velocity solution for different values of parameter χ via computing $\chi\|\mathbf{s}\|_{\ell^2(0,1;L^2(\Omega))}$. The idea is simply based on the following difference quotient for the sensitivity,

$$\mathbf{s} = \frac{\partial \mathbf{u}}{\partial \chi} \approx \frac{\mathbf{u}_{\text{TRM}} - \mathbf{u}_{\text{NSE}}}{\chi}$$

where the solution $\mathbf{u}_{\text{TRM}}$ to the TRM depends on χ while $\mathbf{u}_{\text{NSE}}$ indicates the true solution of Navier–Stokes equations obtained when $\chi = 0$. Tables 3 and 4 show the TRM energy dissipation and $\chi\|\mathbf{s}\|_{\ell^2(0,1;L^2(\Omega))}$ for Reynolds number Re = 10,000 with different values of the relaxation parameter $\chi = 0.01$, 0.1, 1, and 10 as well as different values of the filter length scale $\delta = 0.1$ and 0.01. For both tested δ values, one observes the following:

- Sensitivity quantities, $\chi\|\mathbf{s}\|_{\ell^2(0,1;L^2(\Omega))}$, corresponding to the accuracy of approximated velocity increase as χ values increase from 0.01 to 10.
- An increase in TRM dissipation values, $K(0)-K(t)$, is observed as χ values increase.
- Smaller sensitivity values correspond to smaller values of energy dissipation.
- TRM energy dissipation values are of order $\chi\delta^2$.

For an energy dissipation of order 10^{-4} or less, Table 3 suggests $\chi = 0.01$ while Table 4 provides a larger range of χ values from 0.01 to 1. As a result for a desired order of energy dissipation for a fixed filter length, δ, one can adjust the χ values in such a way that $\chi\delta^2$ is of the same order.

5. Conclusions

In this paper analysis of the energy balance for the time relaxation model, TRM, shows that the average rate of dissipation of energy is enhanced with an additional term multiplied by $\chi\delta^2$. A scaling argument based on the energy cascade leads to a modified Kolmogorov-like 5/3-law for the energy spectrum which is then verified numerically using a spectral-Galerkin computation of a forced time-dependent flow which has reached a state with stationary statistics. It is found that larger values of $\chi\delta^2$ result in more compact energy spectra with a $|k|^{-5/3}$ inertial range that becomes successively more and more abbreviated. At the same time, the energy which accumulates in the forced modes of the simulation is roughly the same for all choices of parameters as is the average rate of energy dissipation. This suggests that the rate at which energy transfers from the forcing range to the inertial range and then to the dissipation range is essentially the same for all values of χ and δ that were considered.

We have further analyzed the convergence of the Oseen type of problem needed for finite-element computations of the time relaxation model. The energy and enstrophy for the TRM are then computed as two essential quantities characterizing change in the structure of the decaying Taylor–Green vortex as well as to test if a simulation of a fluid flow is properly performed. We find a range of values for χ and δ for which the evolution of energy is similar to the NSE as well as values for which the resulting computation shows too much dissipation. In some cases enstrophy increases over time at a rate similar to the evolution of enstrophy in a direct simulations of the NSE; for other choices of parameters the enhanced dissipation results in notably different dynamics.

Our paper ends with a numerical study of the sensitivity equations, again in the context of the Taylor–Green vortex, which measures the accuracy in the approximations obtained from the TRM by computing $\chi\|\mathbf{s}\|$ and time $t = 1$ for various values of χ and δ. Given δ fixed, a range of parameters for χ based on the order of $\chi\delta^2$ are obtained such that the resulting TRM enhancement to the rate of energy dissipation falls within a prescribed limit.

We remark that the filter in the time relaxation model is given by a linear operator with spectral character $\chi\delta^2|k|^2/(1+\delta^2|k|^2)$ which serves to increase the effective viscosity at the large scales while functioning as a damping term at the small scales. In particular, the TRM does not involve higher order differential operators such as hyperviscosity and provides no additional regularization properties that can be used, for example, to show the model is well posed for three-dimensional flows. From a turbulence modeling point of view, since dissipating the small scales is the major role of viscosity, then it is arguably important to have the correct physical viscosity at those scales.

We end with the observation that, even though viscosity plays a lesser role in the dynamics of the large scales, the TRM filter has effects other than those which have been studied. For example, in our scaling analysis of the energy spectrum, certain secondary effects have been represented by the function $\phi(k\delta, \epsilon^{-1/3}k^{-2/3}\chi)$. In the future it would be interesting to characterize the functional form of ϕ that represents the shortening of the inertial range.

Another direction for future work is to use a higher order filter for $\bar{\mathbf{u}}$ such as the d-th order deconvolution operator or an exponential filter. In particular, it would be interesting to consider the cases when the operator L_k appearing in (5) is given

by

$$\nu|k|^2 + \chi\left(\frac{(d+1)\delta^2|k|^2}{1+(d+1)\delta^2|k|^2}\right)^{d+1} \qquad \text{or respectively} \qquad \nu|k|^2 + \chi\exp\left(\frac{-1}{\delta^2|k|^2}\right).$$

Note when $d \geq 1$ these higher order filters satisfy $L_k \approx \nu|k|^2$ both for $|k|$ very small as well as for $|k|$ very large. Thus, only the dissipation in the inertial range would be altered by the corresponding time relaxation model. Exploration of the practical benefits of these higher-order time relaxation models versus the computational complexity provides a possible direction for future research.

References

[1] L.C. Berselli, T. Iliescu and W. Layton, *Mathematics of Large Eddy Simulation of Turbulent Flows*, Scientific Computation, Springer, Berlin, 2006.

[2] M.E. Brachet, D. Meiron, S. Orszag, B. Nickel, R. Morf, and U. Frisch, The Taylor–Green Vortex and Fully Developed Turbulence, *J. of Statist. Phys.*, **34**, 1049–1063, 1984.

[3] S.C. Brenner and L.R. Scott, *The Mathematical Theory of Finite Element Methods*, Springer-Verlag, 1994.

[4] S. Chen, D.D. Holm, L.G. Margolin and R. Zhang, Direct numerical simulation of the Navier–Stokes alpha-model, *Phys. D*, 133, 66–83, 1999.

[5] A. Cheskidov, D.D. Holm, E. Olson and E.S. Titi, On a Leray-alpha Model of Turbulence, *Proc. R. Soc. Long. Ser. A Math. Phys. Eng. Sci.*, 461:2055, 629–649, 2005.

[6] S.M. Cox and P.C. Matthews, Exponential Time Differencing for Stiff Systems, *J. Comput. Phys.*, 176:2, 430-455, 2002.

[7] R. Dascaliuc and Z. Gruijić, Coherent Vortex Structures and 3D Enstrophy Cascade, *Commun. Math. Phys.*, 317, 547–561, 2013.

[8] L. Davis, M. Neda, F. Pahlevani and Jiajia Waters, Fluid Models and Parameter Sensitivities: Computations and Applications, *International Journal of Novel Ideas: Mathematics*, **1**, 12–39, 2017.

[9] S. De, D. Hannasch, M. Neda, E. Nikonova, Numerical analysis and computations of a higher accuracy time relaxation fluid flow model, *Int. J. Comput. Math.*, 89:17, 2353–2373, 2012.

[10] W. Don, D. Gottlieb, C. Shu, O. Schilling, L. Jameson, Numerical Convergence Study of Nearly-Incompressible, Inviscid Taylor–Green Vortex Flow, *Journal of Scientific Computing*, **4**, 1–27, 2005.

[11] A.A. Dunca, M. Neda, Numerical Analysis of a Nonlinear Model of Fluids, *Journal of Mathematical Analysis and Applications* **420**, 1095–1115, 2014.

[12] V.J. Ervin, W.J. Layton, M. Neda, Numerical Analysis of a Higher Order Time Relaxtion Model of Fluids, *International Journal of Numerical Analysis and Modeling*, **4**, 648–670, 2007.

[13] U. Frisch, Turbulence: The Legacy of A. N. Kolmogorov, *Cambridge University Press*, New York, 1995.

[14] M. Germano, Differential filters of elliptic type, *Phys. Fluids*, **29**, 1757–1758, 1986.

[15] B.J. Geurts, Inverse modeling for large eddy simulation, *Phys. Fluids*, **9**, 3585–3587, 1997.

[16] V. John, Large Eddy Simulation of Turbulent Incompressible Flows: Analytical and Numerical Results for a Class of LES Models *Springer-Verlag, New York*, 2004.

[17] F. Hecht, New Development in FreeFem**++**, *J. Numer. Math.*, 10:3–4, 251–265, 2012.

[18] R. Kraichnan, Inertial Ranges in TwoDimensional Turbulence, *Physics of Fluids*, **10**:7 1417–1423, 1967.

[19] A. Labovsky, W. Layton, C. Manica, M. Neda, L. Rebholz, The stabilized extrapolated trapezoidal finite-element method for the Navier–Stokes equations, *Comput. Methods Appl. Mech. Engrg.*, 198:9-12, 958–974, 2009.

[20] W. Layton, *Introduction to the Numerical Analysis of Incompressible Viscous Flows*, Society for Industrial and Applied Mathematics, Philadelphia, PA, 2008.

[21] W. Layton, M. Neda, Truncation of Scales by Time Relaxation, *J. Math Anal. Appl.*, **325**, 788–807, 2007.

[22] W. Layton, C. Manica, M. Neda and L. Rebholz, Numerical Analysis of a high accuracy Leray-deconvolution model of turbulence, *Numerical Methods for Partial Differential Equations*, **24**, 555–582, 2008.

[23] W. Layton and L. Rebholz, *Approximate Deconvolution Models of Turbulence: Analysis, Phenomenology and Numerical Analysis*, Springer Lecture Notes in Mathematics, 2012.
[24] M. Neda, Discontinuous time relaxation method for the time dependent Navier–Stokes equations, *Advances in Numerical Analysis*, **419021**, 1-21, 2010.
[25] M. Neda, F. Pahlevani and J. Waters, Sensitivity Analysis and Computations of the Time Relaxation Model, *Adv. Appl. Math. Mech.*, **7**, 89–115, 2015.
[26] M. Neda and T. Hill, Energy and Enstrophy Investigations in Regularized Navier–Stokes Equations, *VI International Conference of Industrial Engineering and Environmental Protection Proceedings*, 177-182, 2016.
[27] P. Sagaut, *Large Eddy Simulation for Incompressible Flows,* Springer, Berlin, 2001.
[28] S. Stolz, N.A. Adams, L. Kleiser, The approximate deconvolution model for LES of compressible flows and its application to shock-turbulent-boundary-layer interaction, *Phys. Fluids*, **13**, 2985, 2001.
[29] S. Stolz, N.A. Adams, L. Kleiser, An approximate deconvolution model for large eddy simulation with application to wall-bounded flows, *Phys. Fluids*, **13**, 997, 2001.
[30] M.A. Taylor, S. Kurien, G.L. Eyink, Recovering isotropic statistics in turbulence simulations: The Kolmogorov 4/5th law, *Physical Review E*, **68**:2, Article 026310, 2003.
[31] F.M. White, *Fluid Mechanics*, McGraw–Hill Higher Education, 2015.
[32] Y.Y. Yang, D.I. Pullin, Evolultion of vortex-surface fields in viscous Taylor–Green and Kida–Pelz flows, it J. Fluid Mech., 685, 146–164, 2011

Appendix A. The Body Force in the Spectral Simulation

This appendix describes the time-independent body forcing with $\|\mathbf{f}\|_{L^2(\Omega)} = 0.005$ used to drive the computations of the energy spectra given in Section 3.7. It is convenient to assume $\nabla \cdot \mathbf{f} = 0$ or equivalently $k \cdot \mathbf{f}_k = 0$. Since $\mathbf{f}$ is real valued we also have $\mathbf{f}_{-k} = \mathbf{f}_k^*$ where the asterisk represents complex conjugation. This symmetry allows us to describe the forcing used in our simulations my means of a table which lists only half the modes. Specifically, we take

$$\mathbf{f} = \sum_{0<|k|<2} \mathbf{f}_k e^{ik\cdot x} \qquad \text{where} \qquad \mathbf{f}_k = (a_k, b_k, c_k) \times 10^{-5}$$

for the values of a_k, b_k and c_k appearing in Table 5.

TABLE 5. The Fourier modes $\mathbf{f}_k = (a_k, b_k, c_k) \times 10^{-5}$ of the time-independent force $\mathbf{f}$ listed with 5-decimal accuracy omitting terms that can be reproduced using the conjugate symmetry.

k_1	k_2	k_3	$\mathrm{Re}(a_k)$	$\mathrm{Im}(a_k)$	$\mathrm{Re}(b_k)$	$\mathrm{Im}(b_k)$	$\mathrm{Re}(c_k)$	$\mathrm{Im}(c_k)$
0	0	1	1.12230	0.13947	-2.92723	-3.38731	0.00000	0.00000
0	1	0	-1.76374	-3.36666	0.00000	0.00000	-1.00894	-4.52271
0	1	1	-4.47115	-3.02319	2.15459	-1.07705	-2.15459	1.07705
0	-1	1	-3.32541	4.16483	-1.59720	-0.91270	-1.59720	-0.91270
1	0	0	0.00000	0.00000	-3.69666	-4.18476	2.75958	-1.04551
1	0	1	2.83284	-3.48908	3.92105	-2.62899	-2.83284	3.48908
1	1	0	0.31615	-0.69013	-0.31615	0.69013	-2.64386	-0.88762
1	1	1	-0.86208	3.18846	-1.13521	1.53390	1.99729	-4.72236
1	-1	0	2.54484	-3.27935	2.54484	-3.27935	-3.57843	0.57386
1	-1	1	-0.05197	1.63571	0.71261	3.05483	0.76458	1.41912
-1	0	1	-1.58913	-4.25929	-2.99491	3.42326	-1.58913	-4.25929
-1	1	1	-2.75434	-3.42736	-2.64519	-1.59553	-0.10914	-1.83183
-1	-1	1	-1.59139	-3.98616	3.64090	4.96309	2.04950	0.97693

Department of Mathematical Sciences, University of Nevada Las Vegas Las Vegas, NV, 89154, USA
E-mail: hillt12@unlv.edu and monika.neda@unlv.edu

Department of Mathematics and Statistics, University of Nevada Reno, Reno, NV, 89557, USA
E-mail: ejolson@unr.edu

Department of Mathematics, Penn State University Abington, Abington, PA 19001, USA
E-mail: fxp10@psu.edu